

# Measuring the Oblateness and Rotation of Transiting Extrasolar Giant Planets

Jason W. Barnes and Jonathan J. Fortney

*Department of Planetary Sciences, University of Arizona, Tucson, AZ, 85721*

jwbarnes@c3po.lpl.arizona.edu, jfortney@lpl.arizona.edu

## ABSTRACT

We investigate the prospects for characterizing extrasolar giant planets by measuring planetary oblateness from transit photometry and inferring planetary rotational periods. The rotation rates of planets in the solar system vary widely, reflecting the planets' diverse formational and evolutionary histories. A measured oblateness, assumed composition, and equation of state yields a rotation rate from the Darwin-Radau relation. The lightcurve of a transiting oblate planet should differ significantly from that of a spherical one with the same cross-sectional area under identical stellar and orbital conditions. However, if the stellar and orbital parameters are not known *a priori*, fitting for them allows changes in the stellar radius, planetary radius, impact parameter, and stellar limb darkening parameters to mimic the transit signature of an oblate planet, diminishing the oblateness signature. Thus even if HD209458b had an oblateness of 0.1 instead of our predicted 0.003, it would introduce a detectable departure from a model spherical lightcurve at the level of only one part in  $10^5$ . Planets with nonzero obliquity break this degeneracy because their ingress lightcurve is asymmetric relative to that from egress, and their best-case detectability is of order  $10^{-4}$ . However, the measured rotation rate for these objects is non-unique due to degeneracy between obliquity and oblateness and the unknown component of obliquity along the line of sight. Detectability of oblateness is maximized for planets transiting near an impact parameter of 0.7 regardless of obliquity. Future measurements of oblateness will be challenging because the signal is near the photometric limits of current hardware and inherent stellar noise levels.

*Subject headings:* occultations — planets and satellites: general — planets and satellites: individual (HD209458b)

## 1. INTRODUCTION

Discovery of a transiting extrasolar planet, HD209458b (Charbonneau et al. 2000; Henry et al. 2000), has provided one mechanism for researchers to move beyond the discovery and into the characterization of extrasolar planets. Precise *Hubble Space Telescope* measurements of HD209458b's transit lightcurve revealed the radius ( $1.347 \pm 0.060 R_{\text{Jup}}$ ) and orbital inclination ( $86.68^\circ \pm 0.14^\circ$ , from impact parameter 0.508) of the planet, which, along with radial velocity measurements, unambiguously determine the planet's mass ( $0.69 \pm 0.05 M_{\text{Jup}}$ ) and density ( $0.35 \text{ g cm}^{-3}$ ; Brown et al. 2001). Of the over 100 extrasolar planets discovered so far, this large radius makes HD209458b the only one empirically determined to be a gas giant.

Knowledge of a planet's cross-sectional area provides a zeroth order determination of its geometry, and the *HST* photometry is precise enough to constrain the shape of HD209458b to be rounded to first order. While a planet transits the limb of its star, the rate of decrease in apparent stellar brightness is related to the rate of increase in stellar surface area covered by the planet in the same time interval. We investigate whether it is possible to use this information to determine the shape of the planet to second order.

Rotation causes a planet's shape to be flattened, or oblate, by reducing the effective gravitational acceleration at the equator (as a result of centrifugal acceleration) and by redistributing mass within the planet (which changes the gravity field). Oblateness,  $f$ , is defined as a function of the equatorial radius ( $R_{eq}$ ) and the polar radius ( $R_p$ ):

$$f \equiv \frac{R_{eq} - R_p}{R_{eq}}. \quad (1)$$

For Jupiter and Saturn, high rotation rates and low densities result in highly oblate planets:  $f_{\text{Jupiter}} = 0.06487$  and  $f_{\text{Saturn}} = 0.09796$ , compared to  $f_{\text{Earth}} = 0.00335$ .

An earlier investigation of the detectability of oblateness in transiting extrasolar planets was published by Seager & Hui (2002). Our work represents an improvement over Seager & Hui (2002) in the use of model fits to compare oblate and spherical planet transits, the use of the Darwin-Radau relation to associate oblateness and rotation, and a thorough investigation of the degeneracies involved in fitting a transit lightcurve.

In this paper, we investigate the reasons for measuring planetary rotation rates, the relationship between rotation rate and oblateness for extrasolar giant planets, the effect of oblateness on transit lightcurves, and the prospects for determining the oblateness of a planet from transit photometry.

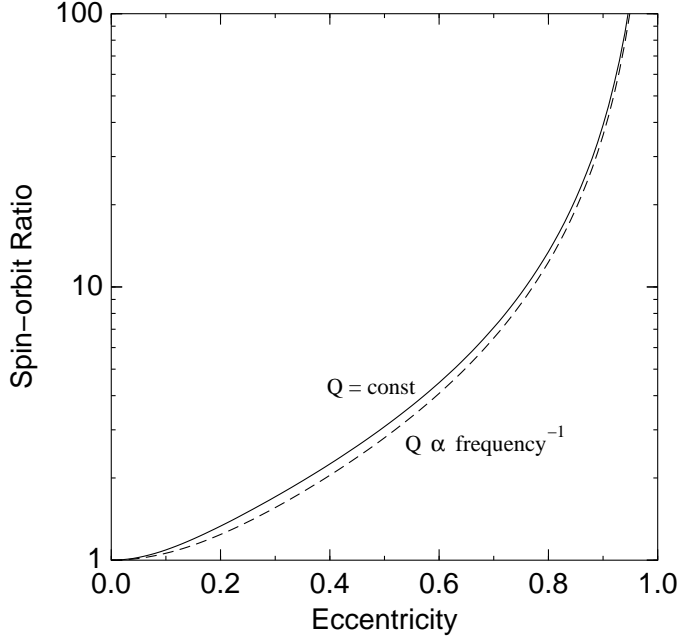


Fig. 1.— Spin to orbital mean motion ratios for tidally evolved fluid planets in equilibrium. The solid line represents the ratio as calculated under the assumption of a frequency-independent tidal dissipation factor  $Q$ , and the dashed line is calculated assuming  $Q \propto \text{frequency}^{-1}$ . Under these assumptions, extremely eccentric planet HD80606b ( $e = 0.93$ ) would, if allowed to come to tidal equilibrium, rotate over 90 times faster than its mean orbital motion!

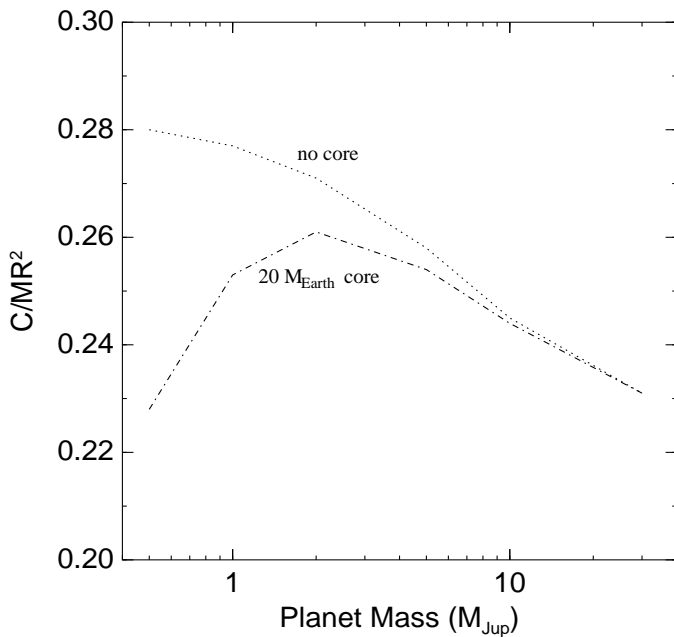


Fig. 2.— The moment of inertia coefficient,  $C$ , as a function of planet mass for hypothetical generic  $1.0 R_{\text{Jup}}$  extrasolar giant planets. Extrasolar giant planets may or may not possess rocky cores depending on their formation mechanism, so we plot  $C$  for both no core (upper curve) and an assumed  $20 M_{\oplus}$  core (lower curve).

## 2. EXOPLANETS AND ROTATION

While knowledge of a planet's mass and radius provides information regarding composition and thermal evolution, measurements of rotation and obliquity promise to constrain the planet's formation, tidal evolution, and tidal dissipation. What these data might reveal about a planet depends on whether the planet is unaffected by stellar tides, slightly affected by tides, or heavily influenced by tides.

### 2.1. Tidally Unaffected

The present-day rotation rate of a planet is the product of both the planet's formation and its subsequent evolution. Planets at sufficiently large distances from their parent stars are not significantly affected by stellar tides, thus these objects rotate with their primordial rates altered by planetary contraction and gravitational interactions between the planet, its satellites, and other planets. To the degree that a planet's rotational angular momentum is primordial, it may be diagnostic of the planet's formation. Planets formed in circular orbits from a protoplanetary disk inherit net prograde angular momentum from the accreting gas, resulting in rapid prograde rotation (Lissauer 1995). Planets that form in eccentric orbits receive less prograde specific angular momentum than planets in circular orbits, and as a result they rotate at rates varying from slow retrograde up to prograde rotations similar to those of circularly accreted planets (Lissauer et al. 1997). Thus, comparing the current-day rotation rates for planets in circular and eccentric orbits may reveal whether extrasolar planets formed in eccentric orbits or acquired their eccentricity later from dynamical interactions with other planets or a disk.

The orientation of a planet's rotational axis relative to the vector perpendicular to the orbital plane, the planet's obliquity or axial tilt  $t$ , can also provide insight into the planet's formation mechanism. Jupiter's low obliquity ( $3.12^\circ$ ) has been suggested as evidence that its formation

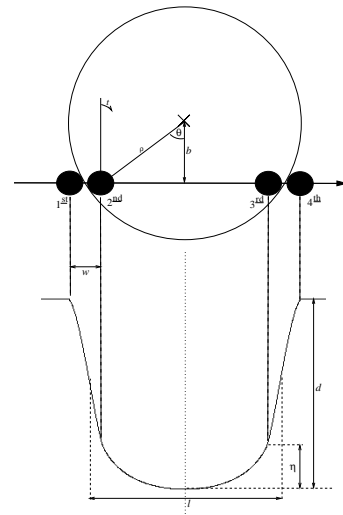


Fig. 3.— Anatomy of a transit, after BCGNB.

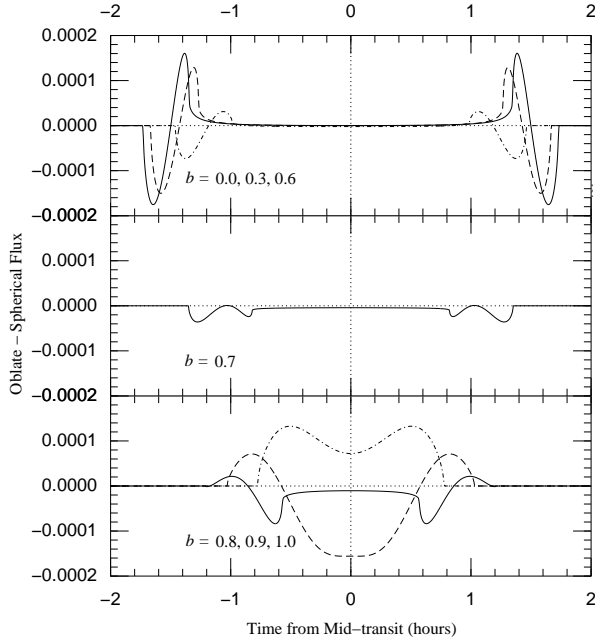


Fig. 4.— Oversimplified model of the effect of oblateness on a transit lightcurve. We plot the differences between the lightcurve of an oblate planet and the lightcurve of a spherical planet with the same cross-sectional area,  $F_{f=0.1}(t) - F_{f=0.0}(t)$  while holding all other transit parameters,  $R_*$ ,  $R_p$ ,  $b$ , and  $c_1$  the same and setting these values equal to those values measured by BCGNB for HD209458b. The top panel plots the lightcurve differential for impact parameters  $b = 0.0$  (solid line),  $b = 0.3$  (dashed line), and  $b = 0.6$  (dot-dashed line). An oblate planet for  $b < 0.7$  encounters first contact before, and second contact after, the equivalent spherical planet, resulting in the initial negative turn for  $F_{f=0.1}(t) - F_{f=0.0}(t)$ , and subsequent positive section of the curve for these impact parameters. In the bottom panel, we plot the differential lightcurve for  $b = 0.8$  (solid line),  $b = 0.9$  (dashed line), and  $b = 1.0$  (dot-dashed line). For  $b > 0.7$ , under otherwise identical conditions, an oblate planet first encounters the limb of the star after the equivalent spherical planet, and last touches the limb later on ingress. For  $b = 0.9$ , because  $R_p > 0.1 R_*$  there is no second contact, i.e. the transit is partial, so the flux differential does not return to near zero, even at mid-transit. The middle plot shows the lightcurve differential at the changeover point between these two regimes, where  $b = 0.7$ .

was dominated by orderly gas flow rather than the stochastic impacts of accreting planetesimals (Lissauer 1993). Tidally unevolved extrasolar planets determined to have high obliquities could be inferred either to have formed differently than Jupiter or to have undergone large obliquity changes as has been suggested for Saturn ( $t = 26.73^\circ$ ; Ward & Hamilton 2002).

## 2.2. Tidally Influenced

Tidal interaction between planets and their parent stars slows the rotation of those planets with close-in orbits (Guillot et al. 1996). This tidal braking continues until the net tidal torque on the planet becomes zero. Whether a planet reaches this end state depends on its age, radius, semimajor axis, and the planet : star mass ratio.

The rate of tidal braking also depends on the parameter  $Q$ , which represents the internal tidal dissipation within the planet. The value of  $Q$  is poorly constrained even for the planets in our own solar system (Goldreich & Soter 1966). Nevertheless, measurements of extrasolar planet rotation rates could constrain  $Q$  for these planets based on the degree of tidal evolution that has taken place (Seager & Hui 2002).

Tidal braking for objects with nonzero obliquity can, somewhat counterintuitively, act to increase an object's obliquity. Tidal torques reduce the component of a planet's angular momentum perpendicular to the orbital plane faster than they reduce the component of the planet's angular momentum in the orbital plane (Peale 1999). This occurs because at solstice the planet's induced tidal bulge is not carried away from the planet's orbital plane by planetary rotation. Therefore for large fractions of the year stellar tidal torques do not act to right the planet's spin axis, while torques that reduce the angular momentum perpendicular to the orbital plane act year-round. As a result, planets that have undergone partial tidal evolution can exhibit temporarily increased obliquity as the planet's rotation rate decreases. Eventually, such a planet reaches maximum obliquity and thereafter approaches synchronous rotation and zero obliquity simultaneously. Planets undergoing tidal evolution may be expected to have higher obliquities on average than planets retaining their primordial obliquity.

## 2.3. Tidally Dominated

The end state of tidal evolution for planets in circular orbits is a 1 : 1 spin-orbit synchronization between the planet's rotation and its orbital period, along with zero obliquity. However, most of the extrasolar planets discovered thus far are on eccentric orbits (Marcy et al. 2000) (we sometimes shorten 'planets on eccentric orbits' to 'eccentric planets' even though the eccentricity is not inherent to the planet). Thus these eccentric planets will never reach 1 : 1 spin-orbit coupling as a result of tidal evolution because the tidal torque (Eq. 2) on the planet from its star is much stronger (due to the  $r^{-6}$  dependence) near periaapsis.

The tidal torque between a planet and star is given by (Murray & Dermott 2000)

$$\tau_{p-*} = -\frac{3}{2} \frac{k_2 G M_*^2 R^5}{Q r^6} \text{sgn}(\Omega - \dot{\phi}), \quad (2)$$

where  $k_2$  is the planet's Love number,  $R$  its radius,  $\Omega$  its rotation rate (in radians per second),  $\dot{\phi}$  the instantaneous orbital angular velocity (also in radians per second), and  $r$  is the instantaneous distance between the planet and star. The function  $\text{sgn}(x)$  is equal to 1 if  $x$  is positive and  $-1$  if  $x$  is negative. The magnitude of the stellar perturbation is proportional to  $GM_*^2$ , the product of the stellar mass ( $M_*$ ) squared and the gravitational constant ( $G$ ). The planet is spun down by tidal torques if its rotation is faster than its orbital motion ( $\Omega > \dot{\phi}$ ), and it is spun up if its rotation is slower than the orbital motion ( $\Omega < \dot{\phi}$ ).

If an eccentric planet were in a 1 : 1 spin-orbit state, it would be spun up by the star when its orbital angular velocity is greater than average near periapsis, and it would be spun down when the orbital angular velocity is low near apoapsis. The total positive tidal torque induced while the planet is in close will exceed the negative torque while it is far away, despite the shorter time spent near periapsis. Thus to be in rotational equilibrium with respect to stellar tides, an eccentric, fluid planet must rotate faster than its mean motion.

The Earth's moon avoids this fate because it has a nonzero component of its quadrupole moment in its orbital plane. The torque that the Earth exerts on this permanent bulge exceeds the net tidal torque imparted on the moon due to its eccentric orbit, keeping the Moon in synchronous rotation (Murray & Dermott 2000). Fluid planets, however, have no permanent quadrupole moment and thus have no restoring torque competing with the stellar tidal torques (Greenberg & Weidenschilling 1984). Tidal evolution ceases for these bodies when the net torque per orbit is zero, which can only be achieved by supersynchronous rotation.

The precise rotation rate necessary to balance the tidal torques over the eccentric orbit depends on how  $Q$  varies with the tidal forcing frequency (the difference between the rotation rate and instantaneous orbital angular velocity,  $\Omega_p - \dot{\phi}_p$ ). Conventionally,  $Q$  has been assumed to be either independent of the forcing frequency or inversely proportional to it (Goldreich & Peale 1968). The resulting equilibrium spin-orbit ratios as a function of eccentricity for each of these cases are plotted in Figure 1.

Probably both of these assumptions for the behavior of  $Q$  are too simple. In particular, if the behavior of  $Q$  changes under a varying tidal forcing frequency ( $\Omega_p - \dot{\phi}_p$  is a function of time), then the tidal equilibrium rotation rate would differ significantly from that plotted in Figure 1. Measurement of rotational rates of eccentric extrasolar planets in tidal equilibrium could, in principle, either differentiate between these two models or suggest other frequency dependences, shedding light on the yet unknown mechanism for tidal dissipation within giant planets.

### 3. ROTATION AND OBLATENESS

Rotation affects the shape of a planet via two mechanisms: gravity must provide centripetal acceleration, thus the higher velocity at the equator causes the planet to bulge by transfer of mass from polar regions; and, secondarily, the redistributed mass alters the planet's gravitational field and attracts even more mass toward the equatorial plane. The ratio of the required centripetal acceleration at the equator to the gravitational acceleration,  $q$ , represents the relative importance of the centripetal acceleration term:

$$q = \frac{\Omega^2 R_{eq}^3}{GM_p}, \quad (3)$$

where  $\Omega$  is the rotation rate in radians per second,  $M_p$  is the mass of the planet, and  $R_{eq}$  is the planet's equatorial radius (Murray & Dermott 2000).

We use the Darwin-Radau relation to relate rotation and oblateness accounting for the gravitational pull of the shifted mass: (Murray & Dermott 2000):

$$\mathbb{C} \equiv \frac{C}{M_p R_{eq}^2} = \frac{2}{3} \left[ 1 - \frac{2}{5} \left( \frac{5}{2} \frac{q}{f} - 1 \right)^{1/2} \right] \quad (4)$$

where  $C$  is the planet's moment of inertia around the rotational axis and  $\mathbb{C}$  is shorthand for  $CM_p^{-1}R_{eq}^{-2}$ . The Darwin-Radau relation is exact for uniform density bodies ( $\mathbb{C} = 0.4$ ), but is only an approximation for gas giant planets ( $\mathbb{C} \sim 0.25$ ; Hubbard 1984).

By combining Equation 3 and Equation 4, we arrive at a relation for rotation rate,  $\Omega$ , as a function of oblateness,  $f$ :

$$\Omega = \sqrt{\frac{fGM_p}{R_{eq}^3} \left[ \frac{5}{2} \left( 1 - \frac{3}{2}\mathbb{C} \right)^2 + \frac{2}{5} \right]}. \quad (5)$$

For our solar system, the Darwin-Radau relation yields rotation periods accurate to within a few percent (Table 1) using model-derived moments of inertia from Hubbard & Marley (1989).

Extending the Darwin-Radau relation to extrasolar planets requires estimation of the appropriate moment of inertia coefficients,  $\mathbb{C}$ , for those planets. For transiting planets whose masses and radii are known, we use a self-consistent hydrodynamic model of the planet and assumptions about its composition to estimate  $\mathbb{C}$  following Fortney & Hubbard (2002). To first order,  $\mathbb{C}$  is independent of oblateness due to similar symmetry around the rotational axis, so our hydrodynamic model does not need to explicitly incorporate oblateness. The Darwin-Radau relation and spherically symmetric hydrodynamic models provide sufficient precision for the current work; however, to estimate the oblateness as a function of rotation more robustly, a two-dimensional interior model involving both rotational and gravitational forces should be used (e.g., Hubbard & Marley 1989).

Under the spherically symmetric assumption, we calculate the  $\mathbb{C}$  of Jupiter to be 0.277 with no core and 0.253

with a  $20 M_{\oplus}$  core, and we calculate the  $\mathbb{C}$  of Saturn to be 0.225 with a core (we are unable to calculate the interior structure of Saturn without a core due to deficiencies in our knowledge of the equation of state). Using these moments of inertia instead of the measured ones listed in Table 1 yields similar rotation errors of a few percent. We apply our model to generic  $1.0 R_{Jup}$  extrasolar giant planets of varying masses and architectures in Figure 2.

For HD209458b, our models calculate  $\mathbb{C}$  to be 0.218 with no core and 0.185 with a  $20 M_{\oplus}$  core. To estimate the oblateness of HD209458b assuming synchronous rotation, we rearrange Equation 5 to solve for  $f$ ,

$$f = \frac{\Omega^2 R^3}{G M_p} \left[ \frac{5}{2} \left( 1 - \frac{3}{2} \mathbb{C} \right)^2 + \frac{2}{5} \right]^{-1}, \quad (6)$$

and then use the synchronous rotation rate  $\Omega = 2.066 \times 10^{-5}$  radians per second to obtain  $f = 0.00285$  with no core and  $f = 0.00256$  with a  $20 M_{\oplus}$  core. These results imply an equator-to-pole radius difference of  $\sim 200$  km, which, although small, is still comparable to the atmospheric scale height at 1 bar,  $\sim 700$  km.

Showman & Guillot (2002) suggest that zonal winds on HD209458b may operate at speeds up to  $\sim 2$  km  $s^{-1}$  in the prograde direction, and Showman & Guillot (2002) go on to show that these winds might then spin up the planet's interior, possibly to commensurate speeds of several hundred  $m s^{-1}$  up to a few  $km s^{-1}$  (though the model of Showman & Guillot (2002) does not treat the outer layers and interior self-consistently). This speed is a non-negligible fraction of the orbital velocity around the planet at the surface,  $30$  km  $s^{-1}$ , and is also comparable to the planet's rotational velocity at the equator,  $2.0$  km  $s^{-1}$ . As such, if radiatively driven winds prove to be important on HD209458b they would affect the planet's oblateness. We use the rotation rate implied by the Showman & Guillot (2002) calculations to provide an upper limit for the expected oblateness of HD209458b. If the entire planet were spinning at its synchronous rate plus  $2$  km  $s^{-1}$  at the cloud tops, the rotational period would be halved to 1.8 days, with a corresponding oblateness of 0.0109 and 0.0098 for the no core and core models respectively.

During revision of this paper, Konacki et al. (2003) announced the discovery of a second transiting planet. This new planet, OGLE-TR-56b, has a radius of  $1.3 R_{Jup}$ , a mass of  $0.9 R_{Jup}$ , and an extremely short orbital period of 1.2 days. Although these parameters are less constrained than those for HD209458b, we proceed to calculate that the oblateness of this new object should be 0.017 with no core and 0.016 with a  $20 M_{\oplus}$  core, for  $\mathbb{C}$  of 0.228 and 0.204 respectively.

Current ground-based transit searches detect low-luminosity objects like brown dwarfs and low-mass stars in addition to planets. However, the high surface gravity for brown dwarfs and lower main sequence stars leads to low values of  $q$  and very small oblatenesses for those objects. For a  $13 M_{Jup}$  brown dwarf with  $1.0 R_{Jup}$  in an HD209458b-like 3.52 day orbit, the expected oblateness is

only 0.00007. Measuring oblateness will therefore only be practical for transiting planets and not for other transiting low-luminosity bodies.

We also note that the measurement of oblateness along with an independent measurement of a planet's rotation rate  $\Omega$  would determine the planet's moment of inertia. This would provide a direct constraint on the planet's internal structure, possibly allowing inferences regarding the planet's bulk helium fraction and/or the presence of a rocky core.

## 4. OBLATENESS AND TRANSIT LIGHTCURVES

### 4.1. Transit Anatomy

Brown et al. (2001) (hereafter BCGNB) investigated the detailed structure of a transit lightcurve while studying the *Hubble Space Telescope* lightcurve of the HD209458b transit. Figure 3 relates transit events to corresponding features in the lightcurve, modeled after BCGNB Figure 4. The flux from the star begins to drop at the onset of transit, known as the first contact. As the planet's disk moves onto the star, the flux drops further, until at second contact the entire planet disk blocks starlight. Third contact is the equivalent of second contact during egress, and fourth contact marks the end of the transit. Due to stellar limb darkening the planet blocks a greater fraction of the star's light at mid-transit than at the second and third contacts, leading to curvature at the bottom of the transit lightcurve.

For a given stellar mass,  $M_*$ , the total transit duration,  $l$ , is a function of the transit chord length and the orbital velocity. We assume a circular orbit, which fixes the planet's orbital velocity. The chord length depends on the stellar radius,  $R_*$ , and the impact parameter,  $b$ . The impact parameter relates to  $i$ , the inclination of the orbital plane relative to the plane of the sky, as

$$b = \frac{|a \cos(i)|}{R_*}, \quad (7)$$

where  $a$  is the semimajor axis of the planet's orbit.

The duration of ingress and egress,  $w$ , is the time between first and second contact, and is a function of  $R_p$ ,  $R_*$ , and  $b$  (or  $i$ ). Transits with  $b \sim 0$  have smaller  $w$  than transits with higher  $b$ . For transits with  $b \sim 1$ , called grazing transits,  $w$  is undefined because there is no second or third contact.

The total transit depth,  $d$ , fixes the ratio  $R_p/R_*$ , where  $R_p$  is the radius of the planet (except in the case of grazing transits).

The magnitude of the curvature at the bottom of the transit lightcurve,  $\eta$ , determines the stellar limb darkening. We use limb darkening parameters  $u_1$  and  $u_2$ , or  $c_1$  and  $c_2$ , which we define mathematically in Section 4.2.

## 4.2. Methods

We calculate theoretical transit lightcurves by comparing the amount of stellar flux blocked by the planet to the total stellar flux. The relative emission intensity across the disk of the star is greatest in the center and lowest along the edges as a result of limb darkening. Many parameterizations of limb darkening exist (see Claret 2000); however, we use the one proposed by BCGNB because it is the most appropriate for planetary transits.

The emission intensity at a given point on the stellar disk,  $I$ , is parameterized as a function of  $\mu = \cos(\sin^{-1}(\rho/R_*))$ , where  $\rho$  is the projected (apparent) distance between the center of the star and the point in question. BCGNB defined a set of two limb darkening coefficients, which we call  $c_1$  and  $c_2$ , that are equivalent to

$$\frac{I(\mu)}{I(1)} = 1 - c_1 \frac{(1 - \mu)(2 - \mu)}{2} + c_2 \frac{(1 - \mu)\mu}{2}. \quad (8)$$

The advantage of this limb darkening function is that  $c_1$  describes the magnitude of the darkening, while  $c_2$  is a correction for curvature. This makes the BCGNB coefficients particularly useful for fitting transit observations because a good fit to data can be achieved by fitting only for the  $c_1$  coefficient.

Our algorithm for calculating the lightcurve takes advantage of the symmetry inherent in the problem: that  $I(\mu)$  depends only on  $\rho$  and not on the angle around the star's center,  $\theta$ . We evaluate the apparent stellar flux at time  $\tau$ ,  $F(\tau)$ , relative to the out-of-transit flux  $F_0$ , by subtracting the amount of stellar flux blocked by the planet from  $F_0$ :

$$F_0 = \int_0^{R_*} 2\pi I(\rho) d\rho, \quad (9)$$

$$F_{\text{blocked}} = \int_0^{R_*} 2\pi I(\rho) x(\rho, \tau) d\rho, \quad (10)$$

and

$$F(\tau) = \frac{F_0 - F_{\text{blocked}}}{F_0}, \quad (11)$$

where  $x(\rho, \tau)$  is the fraction of a ring of radius  $\rho$  and width  $d\rho$  covered by the planet at time  $\tau$ . In effect, we split the star up into infinitesimally small rings and add up the fluxes in Equation 9, then we determine how much of each of these rings is covered by the planet in Equation 10. We calculate the integrals numerically using Romberg's method (Press et al. 1992);  $x(r, t)$  is evaluated numerically as well — there is no closed form general analytical solution to the intersection of an ellipse and a circle.

This algorithm is more efficient than the raster method used by Hubbard et al. (2001) for planets treated as opaque disks because the use of symmetry and Romberg integration minimize the number of computations of the stellar intensity,  $I(\mu)$ .

## 4.3. Results

To illustrate the effect oblateness has on a transit lightcurve, we calculate the difference between the

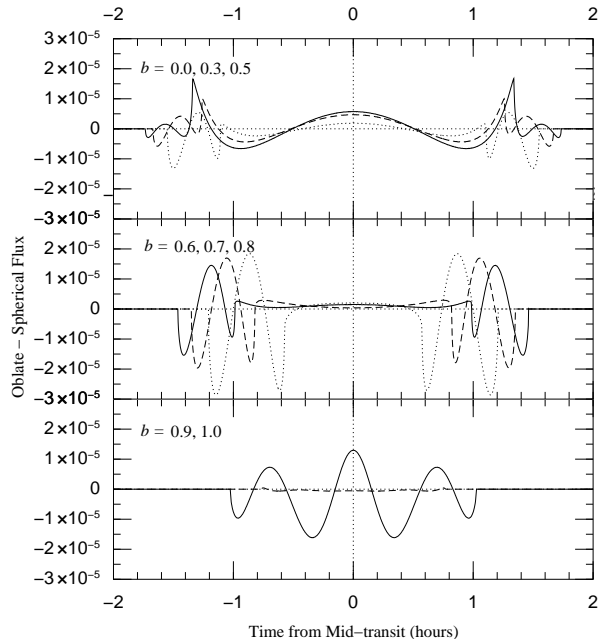


Fig. 5.— Detectable difference between the lightcurve of an oblate ( $f = 0.1$ ) planet and the best-fit spherical model, fitting for  $R_*$ ,  $R_p$ ,  $b$ , and  $c_1$ . Higher  $b$  combined with larger values for  $R_*$  and  $R_p$  simulate the lengthened ingress and egress of an oblate planet, diminishing the difference between oblate and spherical planets from Figure 4 for planets with  $b < 0.7$  (upper panel: solid line,  $b = 0.0$ ; dashed line,  $b = 0.3$ ; dotted line,  $b = 0.5$ ). For planets near  $b = 0.7$ , the length of ingress and egress cannot be simulated by higher  $b$ , and as a result the transit signal is highest for these planets (middle panel: solid line,  $b = 0.6$ ; dashed line,  $b = 0.7$ ; dotted line,  $b = 0.8$ ). Above the critical value,  $b > 0.7$ , the oblate planet's signal can be simulated by lowering  $b$  for the spherical planet fit, reducing the detectability of oblateness (lower panel: solid line,  $b = 0.9$ ; dashed line,  $b = 1.0$ ). It is very difficult to determine the oblateness for planets involved in grazing transits ( $b \sim 1.0$ ). The magnitude of the detectability difference is proportional to  $f$  to first order, hence to estimate the detectability of a planet with arbitrary oblateness, multiply the differences plotted here by  $\frac{f}{0.1} \frac{R_p^2}{R_{HD209458b}^2}$ .

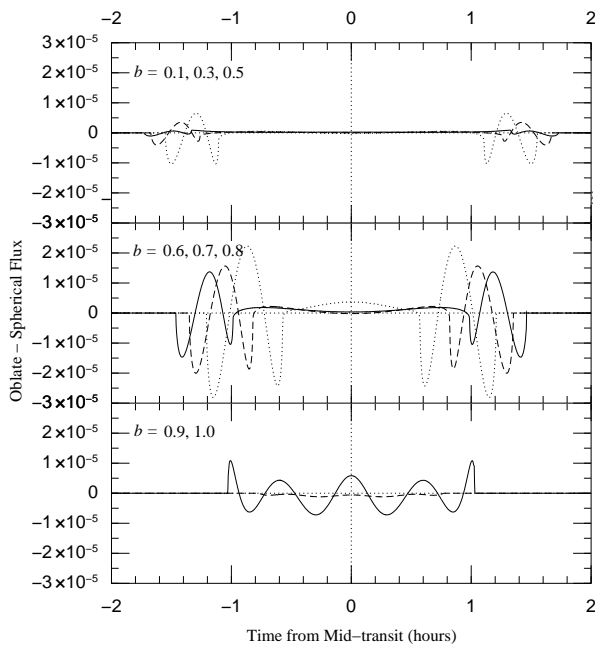


Fig. 6.— Detectable difference between the lightcurve of an oblate ( $f = 0.1$ ) planet and its best-fit spherical model with 5 parameters:  $R_*$ ,  $R_p$ ,  $b$ ,  $c_1$ , and  $c_2$ . As in Figure 5, differing values for  $R_*$ ,  $R_p$ , and  $b$  for a spherical planet transit can allow it to mimic the transit of an oblate planet. With the addition of  $c_2$ , the fit is much better for planets transiting at low impact parameter. (Upper panel: solid line,  $b = 0.0$ ; dashed line,  $b = 0.3$ ; dotted line,  $b = 0.5$ . Middle panel: solid line,  $b = 0.6$ ; dashed line,  $b = 0.7$ ; dotted line,  $b = 0.8$ . Lower panel: solid line,  $b = 0.9$ ; dashed line,  $b = 1.0$ .) The differences for the 5 parameter, like those for the 4 parameter model, vary as  $\frac{f}{0.1} \frac{R_p^2}{R_{HD209458b}^2}$ .

lightcurve of an oblate, zero obliquity planet and that of a spherical planet with the same cross-sectional area. For familiarity, we adopt the transit parameter values measured by BCGNB for the HD209458b transit:  $R_p = 1.347R_{\text{Jup}}$ ,  $R_* = 1.146R_{\odot}$ , and  $c_1 = 0.640$ . Plots of the oblate-spherical differential as a function of impact parameter are shown in Figure 4.

For nearly central transits, an oblate planet encounters first contact before, and second contact after, the equivalent spherical planet. This situation causes the oblate planet’s transit lightcurve initially to dip below that of the spherical planet. However, near the time when the planet center is covering the limb of the star, each planet blocks the same apparent stellar area and the stellar flux difference is zero. As the two hypothetical transits approach second contact, this trend reverses and the spherical planet starts blocking more light than the oblate one until the oblate planet nearly catches up at second contact. Between second and third contacts, the lightcurve differences are slightly nonzero because the two planets cover areas of the star with differing amounts of limb darkening. The lightcurves are symmetric, such that these effects repeat themselves in reverse upon egress.

At high impact parameters (nearly grazing planet transits) the opposite occurs. First contact for the oblate planet occurs after that for the spherical planet, because the point of first contact on the planet is closer to the pole than to the equator. In this scenario, the oblate planet’s transit flux starts higher than, becomes equivalent to, and then drops below that of the spherical planet before returning to near zero for the times between second and third contact. In the case of a grazing transit, this sequence is truncated because there is no second or third contact.

The boundary between these two regions occurs when the local oblate planet radius at the point of first contact is equal to  $R_{ea}$ , the radius of the equivalent spherical planet. For planets that are small compared with the sizes of their stars ( $R_p \ll R_*$ ) and that have low oblateness ( $f \lesssim 0.1$ ), this transition occurs when  $\theta = \pi/4$  (from Figure 3) and  $b = \sqrt{2}/2 = 0.707$ . The flux difference between transits of oblate planets and that for spherical planets, all else being equal, is at a minimum at this point and deviates from zero because the rate of change in stellar area covered is different for the two planets. First, second, third, and fourth contacts all occur at nearly the same time for each planet. However, if all else is not equal, as is usually the case since the stellar parameters are poorly constrained, then this result is misleading and does not represent the detectability of planetary oblateness.

## 5. TRANSIT LIGHTCURVES AND EXOPLANETS

To test whether these flux differences are detectable, we use a Levenberg-Marquardt curve-fitting algorithm adapted from Press et al. (1992) to fit model transits to both the *HST* HD209458b lightcurve and hypothetical model-generated lightcurves by minimizing  $\chi^2$ . As a test,

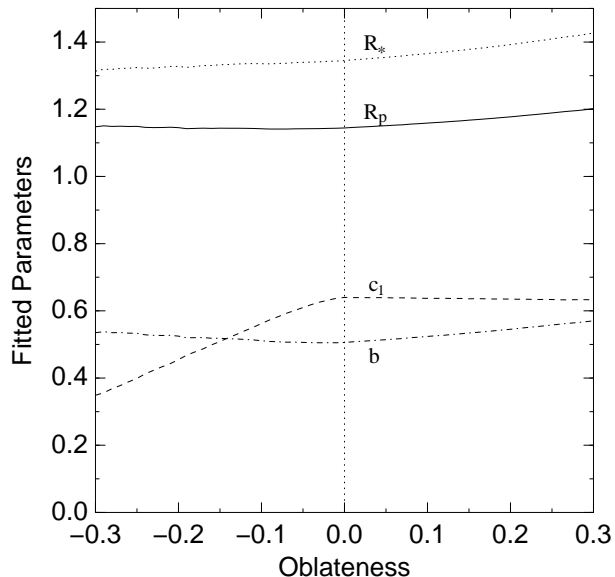


Fig. 7.— Best-fit parameters resulting from fitting a simulated transit lightcurve for a planet with oblateness  $f$  using a spherical planet transit model. Due to the degeneracy in measuring transit parameters  $R_*$ ,  $R_p$ , and  $b$ , and oblateness  $f$ , the best spherical fit to the oblate data have larger radii and higher impact parameters than the actual values (see Section 5.1). Objects with negative values of  $f$  are prolate, a physically unreasonable proposition that we include here for completeness.

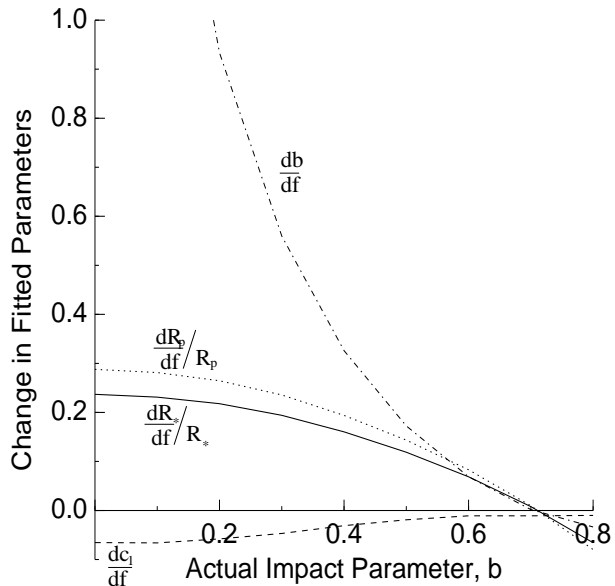


Fig. 8.— Here we plot the change of fitted spherical model parameters with oblateness as a function of impact parameter. The derivative of impact parameter with respect to oblateness continues off the top of this graph to 3.0 at  $b = 0.0$ . An oblate planet with zero obliquity transiting near the center of the star induces much higher deviations of the fitted parameters from the actual parameters than would a planet transiting near the critical impact parameter,  $b = 0.707$ .

we fit the *HST* HD209458b transit lightcurve and obtain  $R_* = 1.142R_\odot$ ,  $R_p = 1.343R_{\text{Jup}}$ ,  $i = 86.72^\circ$  ( $b = 0.504$ ),  $c_1 = 0.647$ , and  $c_2 = -0.065$  with a reduced  $\chi^2$  of 1.05, consistent with the values obtained by BCGNB.

In order for planetary oblateness to have a noticeable effect on a transit lightcurve, it must be distinguishable from the lightcurve of a spherical planet. For a spherical planet transit model, the combination of transit parameters that correspond to the lightcurve that best simulates the data from an actual oblate planet transit become the measured values, and these measured quantities may not be similar to the actual values. Therefore to consider the detectability of planetary oblateness, we compare oblate planet transit lightcurves to those of the best-fit spherical planet lightcurve instead of to the lightcurve of a planet that differs from the actual values only in the oblateness parameter (as we did in Section 4.3).

### 5.1. Zero Obliquity

We compare a model transit of an oblate planet ( $f = 0.1$ ) with zero obliquity, as is the case for a tidally evolved planet, to the transit of the *best-fit* spherical planet in Figure 5 and Figure 6. The oblate planet transit signature is muted in each when compared to Figure 4 due to a degeneracy between the fitted parameters  $R_*$ ,  $R_p$ ,  $b$ , and the oblateness  $f$ . This degeneracy is introduced by the unconstrained nature of the problem: in essence, we are trying to solve for 5 free parameters,  $R_*$ ,  $R_p$ ,  $b$ ,  $c_1$ , and  $f$ , given just 4 constraints,  $d$ ,  $w$ ,  $l$ , and  $\eta$  assuming (as BCGNB did) knowledge of the stellar mass  $M_*$ . Without assuming a value for  $M_*$ , absolute timescales for the problem vanish, yielding a similar conundrum of solving for  $R_p/R_*$ ,  $b$ ,  $c_1$ , and  $f$  given only  $d$ ,  $\eta$ , and  $w/l$ . The previous two sentences are intended only to be simplifications, as at higher photometric precision more information about the conditions of the transit is available. Hereafter we assume knowledge of  $M_*$ , though this analysis could also have been done without this assumption, or with an assumed relation between  $M_*$  and  $R_*$  as proposed by Cody & Sasselov (2002). Changes in  $R_*$ ,  $R_p$ , and  $b$  mimic the signal of an oblate planet by altering the ingress and egress times while maintaining the total transit duration by keeping the chord length constant.

For planets transiting at low impact parameter ( $b < 0.7$ ), an oblate planet's longer ingress and egress (higher  $w$  from Figure 3) are fit better using a spherical model with a higher impact parameter than actual, thus lengthening the time between first and second contact. Since for a given star transits at higher impact parameter have shorter overall duration, the best-fit spherical model has a larger  $R_*$  than the model used to generate the data to maintain the chord length, and thus a larger  $R_p$  to maintain the overall transit depth.

Similarly, for simulated lightcurve data from a transiting oblate planet at high impact parameter ( $b > 0.7$ ), the best-fit spherical model has a lower impact parameter than the simulated planet to increase the duration of ingress and



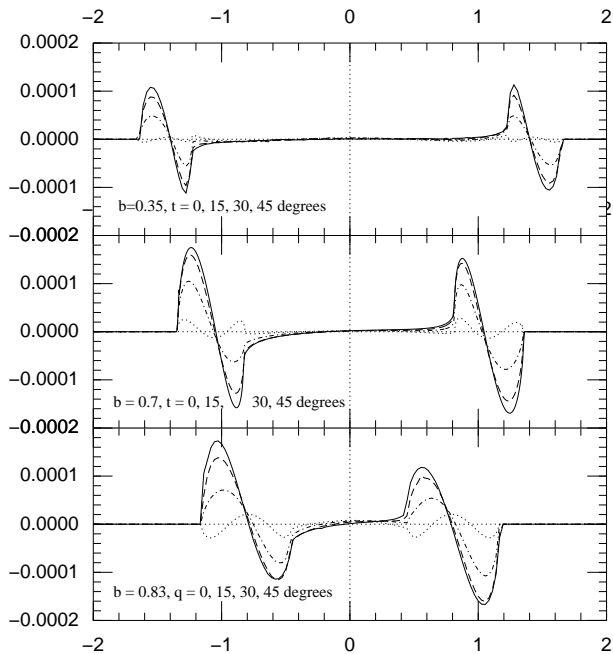


Fig. 9.— Detectability of oblateness and obliquity relative to the best-fit spherical model for planets with nonzero obliquity. The top panel shows the detectability difference for  $b = 0.35$  and  $t = 0^\circ$  (dotted line),  $t = 15^\circ$  (dot-dashed line),  $t = 30^\circ$  (dashed line), and  $t = 45^\circ$  (solid line). The middle panel represents the same varying obliquities calculated for  $b = 0.7$ , and the bottom panel shows the differences for  $b = 0.83$ . The shape of the difference is qualitatively similar for each case. The difference is maximized for  $t = 45^\circ$  and  $b = 0.7$ , and falls off as the parameters near  $t = 0^\circ$ ,  $t = 90^\circ$ ,  $b = 0.0$ , and  $b = 1.0$ . Due to the symmetry of the problem, obliquities the ones shown plus  $90^\circ$  are the time inverse of the differences shown.

egress. For these planets, the fitted spherical parameters have smaller  $R_*$  and  $R_p$  than the simulated planet to maintain the character of the rest of the lightcurve.

Oblate planets that have impact parameters near the critical value,  $b \sim 0.7$ , cannot be as easily fit using a spherical model because changes in the impact parameter of the fit cannot increase the duration of ingress and egress. For these planets, the difference between the oblate planet transit lightcurve and the best-fit spherical planet transit lightcurve is maximized, providing the largest possible photometric signal with which to measure oblateness.

At present, it is necessary to fit for  $R_*$  and stellar limb-darkening parameters because of our limited knowledge of these values for the host stars of transiting planets. If  $R_*$  were known to sufficient accuracy (less than 1%), then with knowledge of  $M_*$  the degeneracy between  $R_*$ ,  $R_p$ , and  $b$  would be broken, allowing measurement of planetary oblateness without fitting. However, without assumptions about the stellar mass, knowledge of  $R_*$  would only help to constrain  $M_*$ . Cody & Sasselo (2002) show that, for the star HD209458, current evolutionary models combined with transit data serve to measure the stellar radius to a precision of only 10%.

In Figure 5 we plot the difference between the transit lightcurve of a hypothetical planet with the characteristics of HD209458b but an oblateness  $f = 0.1$ , and that planet's best-fit spherical model fitting for  $R_*$ ,  $R_p$ ,  $b$ , and  $c_1$ . For low values of the impact parameter,  $b \leq 0.5$ , the best-fit spherical lightcurve emulates the oblate planet's ingress and egress while leaving a subtly different transit bottom due to the planet traversing a differently limb-darkened chord across the star. The magnitude of the difference is approximately a factor of 10 smaller than the non-fit difference from Figure 4. Near the critical impact parameter,  $b = 0.7$ , the transit lightcurve bottoms are very similar since the best-fit  $b$  is very similar to the actual oblate planet's impact parameter; however, the ingress and egress differ in flux by a few parts in  $10^5$  for  $f = 0.1$ . For grazing transits,  $b \sim 1.0$ , the best-fit spherical model's lightcurve is indistinguishable from the oblate planet transit lightcurve even at the  $10^{-6}$  relative accuracy level.

Figure 6 shows the same differences as in Figure 5, but with a second stellar limb darkening parameter, BCGNB's  $c_2$ , also left as a free parameter in the fit. Including  $c_2$  in the fit allows the fitting algorithm to match the transit bottom (the time between second and third contacts) better. This effect leads to excellent fits of oblate planet transits using spherical planet models and reduces the detectable difference to less than one part in  $10^5$  for  $0.0 < b < 0.5$  and  $b > 0.9$  using HD209458 stellar and planetary radii and an oblateness of  $f = 0.1$ . For  $b = 0.0$  and  $b = 1.0$  the spherical model emulates an oblate transit particularly well, with the differences between the two being only a few millionths of the stellar flux.

In both the 4- and 5-parameter zero-obliquity models, it is easiest to measure the effects of oblateness on the transit light curve for transits near the critical impact parameter.

For HD209458 values with  $f = 0.1$ , the oblateness signal then approaches  $3 \times 10^{-5}$  for tens of minutes during ingress and egress and peaks near  $b = 0.8$  instead of the critical value of  $b = 0.7$  due to the finite radius of HD209458b relative to its parent star.

Based on observations of the Sun, Borucki et al. (1997) expect the intrinsic stellar photometric variability on transit timescales to be  $\sim 10^{-5}$ . Jenkins (2002) used 5 years of 3 minute resolution SOHO spacecraft data to deduce the noise power spectrum of the Sun. These noise effects are close enough in magnitude to the transit signal so as to affect the detectability of a transiting oblate planet.

Future high-precision space-based photometry missions such as MOST and Kepler may be able to detect the effect for highly oblate transiting extrasolar planets, but the S/N ratio could be so low as to make unambiguous measurements of oblateness difficult to obtain.

If an observer were to fit photometric timeseries data from a transit of an oblate planet without fitting explicitly for the oblateness  $f$  (as, for instance, if the precision is insufficient to measure  $f$ ), the planet's oblateness will be manifest as an astrophysical source of systematic error in the determination of the other transit parameters. Figure 7 shows the effect that oblateness has on the stellar radius, planetary radius, impact parameter, and limb darkening coefficient for HD209458b. This variation is a strong function of the planet's impact parameter. In Figure 8, we show how this systematic variation changes as a function of the initial impact parameter for the HD209458b system. As a severe but still physical example, an HD209458b-like planet with oblateness  $f = 0.1$  that transits at  $b = 0.0$  would be measured to have radii 2% above actual and an impact parameter nearly 0.3 above the real impact parameter.

#### 5.1.1. HD209458b

To illustrate the robustness of the degeneracy between  $R_*$ ,  $R_p$ ,  $b$ , and  $f$  discussed in Section 5.1, we fit the *HST* lightcurve from BCGNB using a planet with a fixed, large oblateness of 0.3(!). The best-fit parameters were  $R_* = 1.08 R_\odot$ ,  $R_p = 1.26 R_{Jup}$ ,  $b = 0.39$ , and  $c_1 = 0.633$  with a reduced  $\chi^2 = 1.06$  — indistinguishable in significance from the spherical planet model! Although unlikely, a high actual oblateness for HD209458b could alter the measured value for the planet's radius into better agreement with theoretical models.

The expected detectability of oblateness for HD209458b is extremely low. During ingress and egress the transit lightcurve for HD209458b should differ from that of the best-fit spherical model by only one part in  $10^6$  for  $f = 0.01$  and at the level of  $3 \times 10^{-7}$  if  $f = 0.003$ . For comparison, the BCGNB *HST* photometric precision is  $1 \times 10^{-4}$ .

Although the systematic error in the determination of transit parameters can be important for highly oblate planets, it is not at all significant for HD209458b. Assuming HD209458b has an oblateness of  $f = 0.003$  as calculated in

Section 3, the fitted radii are only  $\sim 0.05\%$  above the actual radii, and the fitted impact parameter is 0.0006 above what the actual impact parameter should be.

#### 5.1.2. OGLE-TR-56b

Measuring the oblateness of the new transiting planet OGLE-TR-56b (Konacki et al. 2003),  $f = 0.016$  (see Section 3), would require photometric precision down to at least  $4 \times 10^{-6}$ . Since the impact parameter for this object is as yet unconstrained, the above precision corresponds to  $b = 0.7$ . For other transit geometries, higher precision photometry would be necessary to measure the oblateness of this object.

### 5.2. Nonzero Obliquity

We plot the detectability of oblateness and obliquity for planets with nonzero obliquity in Figure 9. Here we define the projected obliquity (which we refer to as just obliquity hereafter), or axial tilt  $t$ , as the angle between the orbit angular momentum vector and the rotational angular momentum vector projected into the sky plane, measured clockwise from the angular momentum vector (see Figure 3). The major effect of nonzero obliquity is to introduce an asymmetry into the transit lightcurve (Hui & Seager 2002).

The plots in Figure 9 are difference plots for planets with different obliquities and impact parameters, yet all have the same shape qualitatively. In trying to fit the asymmetric ingress and egress lightcurves, the best-fit spherical planet splits the difference between them. For planets with  $0 < t < \pi/2$ , this process yields a difference curve that initially increases as the spherical planet covers the star at a faster rate than does the oblate planet. Because of the asymmetric nature of the problem, however, the egress of the oblate planet takes longer than the spherical one, causing an initial upturn near third contact. The transit lightcurve difference for planets with  $0 > t > -\pi/2$  is equal to the one for  $0 < t < \pi/2$ , but reversed in time.

This general shape is the same for the asymmetric component of each transit lightcurve, and it is superimposed on top of the symmetric component studied in Section 5.1. The asymmetric component is maximized near the critical impact parameter ( $b = 0.7$ ), because the planet crosses the stellar limb with its projected velocity vector at an angle of  $\pi/4$  with respect to the limb. For transits across the middle of the star,  $b = 0$ , the asymmetric component of the lightcurve vanishes as a new symmetry around the planet's path is introduced, and the local angle between the velocity vector and the limb is  $\pi/2$ . Similarly the asymmetric planet signal formally goes to zero for grazing transits at  $b = 1.0$ , but in practice the asymmetric component is still high for Jupiter-sized planets.

Planets with obliquities of zero ( $t = 0$ ) are symmetric and have no asymmetric lightcurve component (see Section 5.1). Likewise, planets with  $t = \pi/2$  are also symmetric. The asymmetric component is maximized for planets with

$$t = \pi/4.$$

Transiting planets with nonzero obliquity can break the degeneracy between transit parameters discussed in Section 5.1. However, when the obliquity is nonzero a degeneracy between projected obliquity and oblateness is introduced: a measured asymmetric lightcurve component of a given magnitude could be due to a planet with low oblateness but near the maximum detectability obliquity of  $t = \pi/4$ , or it could be the result of a more highly oblate planet with a lower obliquity. In this case only a lower limit to the oblateness can be determined based on the oblateness for an assumed obliquity of  $\pi/4$ . This degeneracy can be broken with measurements precise enough to determine the symmetric lightcurve component. In addition, transit photometry is only able to measure the projected oblateness and obliquity of such objects due to the unknown component of obliquity along the line-of-sight (Hui & Seager 2002), therefore the true oblateness is never smaller than the measured, projected oblateness.

The asymmetric transit signal of an oblate planet with nonzero obliquity could also be muddled by the presence of other bodies orbiting the planet. Orbiting satellites or rings could both introduce asymmetries into the transit lightcurve that may not be easily distinguishable from the asymmetry resulting from the oblate planet. Satellites around tidally evolved planets are not stable (Barnes & O'Brien 2002), and rings around these objects may prove to be difficult to sustain as well. However, objects that are not tidally evolved, those farther away from their parent stars, may potentially retain such adornments, and their effects on a transit lightcurve could be difficult to differentiate from oblateness.

Orbital eccentricity can also cause a transit lightcurve to be asymmetric. Although the eccentricity of HD209458b is zero to within measurement uncertainty based on radial velocity measurements, future planets discovered solely by their transits may not have constrained orbital parameters. For these objects with unknown eccentricity, if the eccentricity is very high then under some conditions the velocity change between ingress and egress may be high enough to emulate the oblateness asymmetry discussed in this section. However, we do not explicitly treat that situation in this paper.

## 6. CONCLUSIONS

Examining a transiting planet's precise lightcurve can allow the measurement of the planet's oblateness and, therefore, rotation rate, beginning the process of characterizing extrasolar planets. To a reasonably close approximation (a few percent), the rotation rate of an extrasolar giant planets is related to the planet's oblateness by the Darwin-Radau relation. Measurements of a planet's rotation rate could constrain the tidal dissipation factor  $Q$  for those planets, as well as possibly shed light on the tidal dissipation mechanism within giant planets based on the spin : orbit ratios of tidally evolved eccentric planets.

The detectable effect of oblateness on the lightcurve of a planet with zero obliquity is at best on the level of a few parts in  $10^5$ . This effect may be discernable from space with ultra high precision photometry, but could prove to be indistinguishable from stellar noise or other confounding effects. Accurate independent measurements of stellar radius can break the degeneracy between the stellar radius, planetary radius, and impact parameter, allowing for much easier measurement of oblateness. Without such measurements, the primary effect of oblateness and zero obliquity when studying transit lightcurves will be to provide an astrophysical source of systematic error in the measurement of transit parameters.

Planets with nonzero obliquity have higher detectabilities (up to  $\sim 10^{-4}$ ) than planets with no obliquity, but yield nonunique determinations of obliquity and oblateness. In order to obtain unique obliquities and oblatenesses for these objects, precision comparable to that needed for the zero obliquity case is needed.

The detectability of oblateness for transiting planets is maximized for impact parameters near the critical impact parameter of  $b = 0.7$ . Many transit searches are currently underway, yielding the potential for the discovery of many transiting planets in coming years. Given the opportunity to attempt to measure oblateness, our analysis suggests that the optimal observational target selection strategy would be to observe planets around bright stars that transit near an impact parameter of 0.7.

The authors wish to acknowledge Bill Hubbard and Fred Ciesla for useful conversations; Wayne Barnes, Robert H. Brown, Christian Schaller, and Paul Withers for manuscript suggestions; and Robert H. Brown for valuable advice.

## REFERENCES

Ward, W. R. & Hamilton, D. P. 2002, BAAS, 34

- Barnes, J. W. & O'Brien, D. P. 2002, ApJ, 575, 1087
- Borucki, W. J., Koch, D. G., Dunham, E. W., & Jenkins, J. M. 1997, in ASP Conf. Ser. 119, 153
- Brown, T. M., Charbonneau, D., Gilliland, R. L., Noyes, R. W., & Burrows, A. 2001, ApJ, 552, 699
- Charbonneau, D., Brown, T. M., Latham, D. W., & Mayor, M. 2000, ApJ, 529, L45
- Claret, A. 2000, A&A, 363, 1081
- Cody, A. M. & Sasselov, D. D. 2002, ApJ, 569, 451
- Fortney, J. & Hubbard, W. 2002, Icarus
- Goldreich, P. & Peale, S. J. 1968, ARA&A, 6, 287
- Goldreich, P. & Soter, S. 1966, Icarus, 5, 375
- Greenberg, R. & Weidenschilling, S. J. 1984, Icarus, 58, 186
- Guillot, T., Burrows, A., Hubbard, W. B., Lunine, J. I., & Saumon, D. 1996, ApJ, 459, L35
- Henry, G. W., Marcy, G. W., Butler, R. P., & Vogt, S. S. 2000, ApJ, 529, L41
- Hubbard, W. B. 1984, Planetary Interiors (New York: Van Nostrand Reinhold Co.)
- Hubbard, W. B., Fortney, J. J., Lunine, J. I., Burrows, A., Sudarsky, D., & Pinto, P. 2001, ApJ, 560, 413
- Hubbard, W. B. & Marley, M. S. 1989, Icarus, 78, 102
- Hui, L. & Seager, S. 2002, ApJ, 572, 540
- Jenkins, J. M. 2002, ApJ, 575, 493
- Konacki, M., Torres, G., Jha, S., & Sasselov, D. 2003, Nature
- Lissauer, J. J. 1993, ARA&A, 31, 129
- . 1995, Icarus, 114, 217
- Lissauer, J. J., Berman, A. F., Greenzweig, Y., & Kary, D. M. 1997, Icarus, 127, 65
- Marcy, G. W., Cochran, W. D., & Mayor, M. 2000, in Protostars and Planets IV. (Tucson: University of Arizona Press), 1285
- Murray, C. D. & Dermott, S. F. 2000, Solar System Dynamics (New York: Cambridge University Press)
- Peale, S. J. 1999, ARA&A, 37, 533
- Press, W. H., Teukolsky, S. A., Vetterling, W. T., & Flannery, B. P. 1992, Numerical recipes in C. The art of scientific computing (Cambridge: University Press)
- Seager, S. & Hui, L. 2002, ApJ, 574, 1004
- Showman, A. P. & Guillot, T. 2002, A&A, 385, 166

TABLE 1  
DARWIN-RADAU IN THE SOLAR SYSTEM

Planet	f	$\mathbb{C}$	Calculated Period	Actual Period	Error
Jupiter	0.06487	0.26401 <sup>1</sup>	10.1609 hr	9.92425 hr	2.38%
Saturn	0.09796	0.22037 <sup>1</sup>	10.8817 hr	10.6562 hr	2.12%
Uranus	0.02293	0.2268 <sup>1</sup>	16.6459 hr	17.24 hr	3.45%
Neptune	0.01708	0.23 *	16.8656 hr	16.11 hr	4.69%
Earth	0.00335	0.3308	23.8808 hr	23.9342 hr	0.223%

<sup>1</sup>Hubbard & Marley (1989)

\* Assumed

NOTE.— Comparison of calculated rotation rates from the Darwin-Radau approximation (Equation 4) to actual rotation rates for selected planets in our solar system.